

# Processing properties of ON and OFF pathways for *Drosophila* motion detection

Rudy Behnia<sup>1</sup>, Damon A. Clark<sup>2,3</sup>, Adam G. Carter<sup>4</sup>, Thomas R. Clandinin<sup>3</sup> & Claude Desplan<sup>1,5</sup>

The algorithms and neural circuits that process spatio-temporal changes in luminance to extract visual motion cues have been the focus of intense research. An influential model, the Hassenstein–Reichardt correlator<sup>1</sup>, relies on differential temporal filtering of two spatially separated input channels, delaying one input signal with respect to the other. Motion in a particular direction causes these delayed and non-delayed luminance signals to arrive simultaneously at a subsequent processing step in the brain; these signals are then nonlinearly amplified to produce a direction-selective response. Recent work in *Drosophila* has identified two parallel pathways that selectively respond to either moving light or dark edges<sup>2,3</sup>. Each of these pathways requires two critical processing steps to be applied to incoming signals: differential delay between the spatial input channels, and distinct processing of brightness increment and decrement signals. Here we demonstrate, using *in vivo* patch-clamp recordings, that four medulla neurons implement these two processing steps. The neurons Mi1 and Tm3 respond selectively to brightness increments, with the response of Mi1 delayed relative to Tm3. Conversely, Tm1 and Tm2 respond selectively to brightness decrements, with the response of Tm1 delayed compared with Tm2. Remarkably, constraining Hassenstein–Reichardt correlator models using these measurements produces outputs consistent with previously measured properties of motion detectors, including temporal frequency tuning and specificity for light versus dark edges. We propose that Mi1 and Tm3 perform critical processing of the delayed and non-delayed input channels of the correlator responsible for the detection of light edges, while Tm1 and Tm2 play analogous roles in the detection of moving dark edges. Our data show that specific medulla neurons possess response properties that allow them to implement the algorithmic steps that precede the correlative operation in the Hassenstein–Reichardt correlator, revealing elements of the long-sought neural substrates of motion detection in the fly.

Behavioural and electrophysiological studies in flies have demonstrated that visual motion responses display the fundamental signatures predicted by the Hassenstein–Reichardt correlator (HRC)<sup>1,4,5</sup>. In *Drosophila*, photoreceptors R1–R6 are required for motion detection, and synapse onto three lamina monopolar cells L1, L2 and L3 (ref. 6), which provide inputs to distinct motion pathways<sup>2,3,7–11</sup>. L1 feeds into pathways involved in detecting moving light edges<sup>2,3</sup> while L2, with contributions from L1 and L3, is involved in detecting moving dark edges<sup>2,3,10</sup> (Fig. 1b). Deeper in the optic lobe, two direction-selective neuronal types, T4 and T5, are also differentially tuned: T4 cells respond to moving light edges while T5 cells respond to moving dark edges<sup>12</sup>. Both T4 and T5 are required for downstream, direction-selective responses of the visual system output cells called lobula plate tangential cells (LPTCs), and are themselves direction selective. T4 neurons respond selectively to moving light edges and T5 neurons respond to moving dark edges. Mi1 and Tm3 are the main postsynaptic targets of L1 while Tm1 and Tm2 are the main postsynaptic targets of L2. The axons of Mi1 and Tm3 contact T4 in the most proximal medulla layer, whereas Tm1 and Tm2 contact T5 dendrites in superficial lobula layers (modified from ref. 30). c, *In vivo* electrophysiology set up: a window is cut in a dorsal region of the head cuticle of an immobilized live fly to expose the cell bodies of medulla neurons to a glass pipette used to perform the recordings. Grey-scale images are displayed on a screen positioned in front of the fly, using a digital light projector coupled to a coherent fibre optic bundle.

Since L1 and L2 relay information about both contrast increments and decrements<sup>3</sup> (they hyperpolarize in response to light increments and depolarize in response to decrements) and act as inputs to motion pathways, we focused on medulla neurons that link L1 and L2 to T4 and T5 to identify potential sites of half-wave rectification and delay. Electron microscopic reconstruction of the medulla has identified columnar neurons types Tm3 and Mi1 as receiving the large majority of synapses

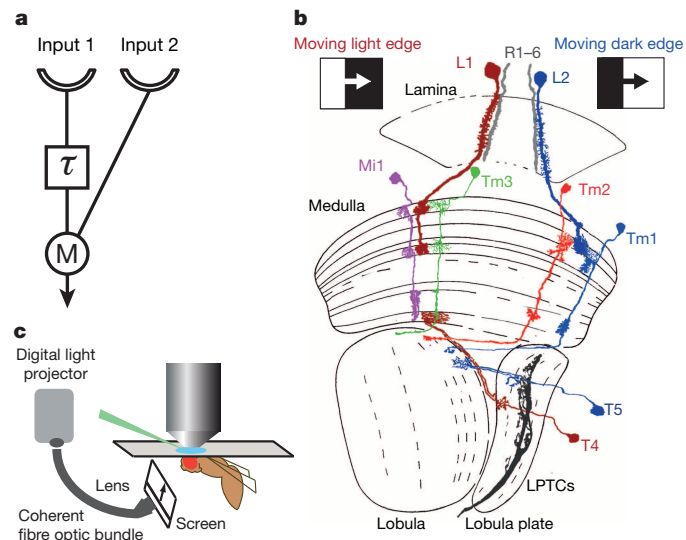


**Figure 1 | Motion detection and the fly optic lobe.** a, A half HRC sensitive to rightward motion. An object moving from left to right first activates input 1 and then input 2. The signal from input 1 is delayed ( $\tau$ ) and arrives at the correlation stage (M for multiplication) close in time to the signal from unit 2, nonlinearly enhancing the signal. For leftward motion, the signals are separated in time by the delay and no motion signal is generated. In the full correlator model, two mirror symmetric correlators are subtracted, producing responses that have opposite signs for opposite directions (see Fig. 4a). b, Light edge (L1) and dark edge (L2) motion-sensitive pathways in the *Drosophila* optic lobe. L1 and L2 lamina monopolar cells in the lamina provide inputs to two distinct motion-sensitive pathways that selectively respond to moving light edges and dark edges, respectively. L1 and L3 also contribute to the pathway detecting moving dark edge (not shown). T4 and T5 in the lobula complex are the main inputs to lobula plate tangential cells (LPTCs), and are themselves direction selective. T4 neurons respond selectively to moving light edges and T5 neurons respond to moving dark edges. Mi1 and Tm3 are the main postsynaptic targets of L1 while Tm1 and Tm2 are the main postsynaptic targets of L2. The axons of Mi1 and Tm3 contact T4 in the most proximal medulla layer, whereas Tm1 and Tm2 contact T5 dendrites in superficial lobula layers (modified from ref. 30). c, *In vivo* electrophysiology set up: a window is cut in a dorsal region of the head cuticle of an immobilized live fly to expose the cell bodies of medulla neurons to a glass pipette used to perform the recordings. Grey-scale images are displayed on a screen positioned in front of the fly, using a digital light projector coupled to a coherent fibre optic bundle.

<sup>1</sup>Center for Developmental Genetics, Department of Biology, New York University, New York, New York 10003-6688, USA. <sup>2</sup>Department of Molecular, Cellular, and Developmental Biology, Yale University, New Haven, Connecticut 06511, USA. <sup>3</sup>Department of Neurobiology, Stanford University, Stanford, California 94305, USA. <sup>4</sup>Center for Neural Science, New York University, New York, New York 10003, USA.

<sup>5</sup>Center for Genomics & Systems Biology, New York University Abu Dhabi Institute, Abu Dhabi, United Arab Emirates.

from L1 (refs 15, 16). Similarly, Tm1 and Tm2 are the main synaptic targets of L2 (refs 15, 16). Furthermore, Mi1 and Tm3 together constitute over 80% of the presynaptic inputs to T4 (ref. 16) and both Tm1 and Tm2 provide input to T5 (ref. 17). Based on their innervation patterns, Mi1 and Tm3 have been proposed to be core components of the motion detector for light edges involving T4 (ref. 16). Similarly, Tm1 and Tm2 are likely candidates for analogous roles in a motion detector for dark edges.

Since changes in luminance are central to motion detection, we first examined the responses of Mi1, Tm3, Tm1 and Tm2 to step changes in light intensity by performing whole-cell current-clamp recordings on awake immobilized fruit flies (Fig. 1c). Both Mi1 and Tm3 responded with a strong, transient depolarization at the onset of a 1 s light step, and then transiently hyperpolarized to below pre-stimulus levels at light offset (Fig. 2a right and Extended Data Fig. 1a). The responses to onset and offset of light differed in magnitude: in Mi1, the offset hyperpolarization amplitude was only 11% (s.e.m. = 3.5%) of the onset depolarization, while in Tm3 this fraction was 36.6% (s.e.m. = 7.1%) (Extended Data Fig. 1c). A brief flash of light (200 ms) elicited a sharper depolarization in both cells, with the offset hyperpolarization terminating the depolarization phase of the response (Fig. 2a left). The responses observed in Tm1 and Tm2 were similar to each other, yet were strikingly different from those in Mi1 and Tm3 (Fig. 2b and Extended Data Fig. 1b). Tm1 and Tm2 hyperpolarized at light onset, and depolarized strongly at light offset. The hyperpolarization of Tm1 evoked by stimulus onset was 26.1% (s.e.m. = 3.8%) as large as the depolarization evoked at offset; for Tm2, this number was 17.7% (s.e.m. = 2.3%) (Extended Data Fig. 1c). Finally,

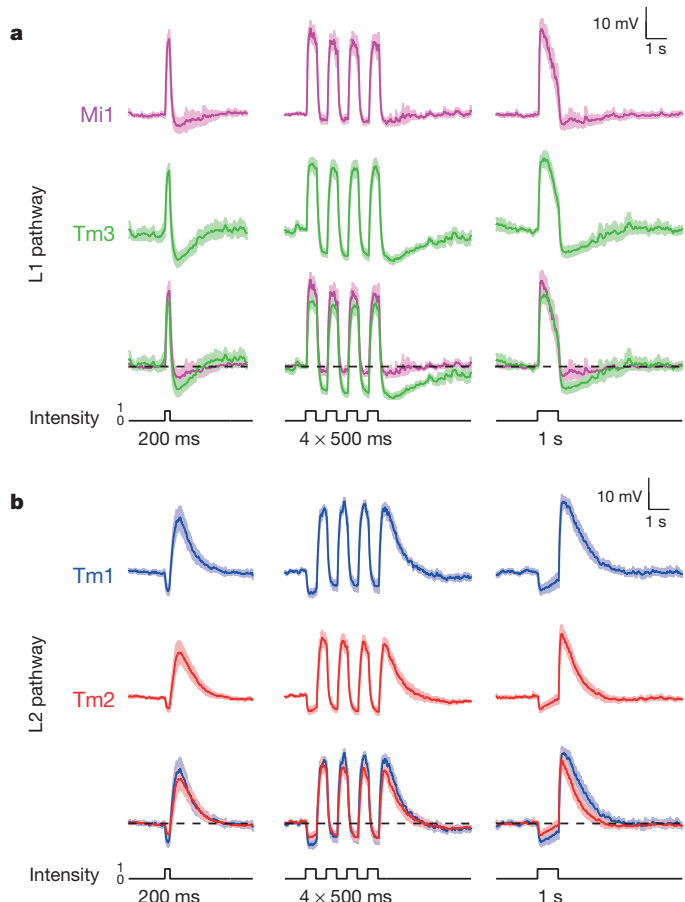


**Figure 2 | Mi1/Tm3 respond selectively to brightness increments while Tm1/Tm2 respond selectively to brightness decrements.** **a**, Average evoked responses of Mi1 ( $n = 7$ ) and Tm3 ( $n = 10$ ) in the L1 pathway, in response to 200 ms, four consecutive 500 ms and 1 s full-field flashes of light from dark. Thick lines indicate the mean; shaded region indicates s.e.m. **b**, Averaged evoked responses ( $\pm$  s.e.m.) of Tm1 ( $n = 10$ ) and Tm2 ( $n = 11$ ) in the L2 pathway in response to the same stimuli.

rapid sequential presentations of light caused repolarization of these cells while their membrane potential was still peaking or decaying from a previous flash (Fig. 2b middle). Thus, Mi1 and Tm3, the postsynaptic targets of L1, respond mostly to brightness increments. Conversely, Tm1 and Tm2, the postsynaptic targets of L2, respond most strongly to brightness decrements, consistent with calcium imaging studies of Tm2 (ref. 18). All four cells showed asymmetries in their responses to brightness changes, consistent with a role in conferring edge selectivity to each pathway. In addition, we examined whether these medulla neurons could relay long-term information about contrast to downstream circuitry by characterizing responses evoked by 5 s brightness increments or decrements presented on an intermediate grey background (Extended Data Fig. 2a–d). All four neurons displayed a sustained response for both brightness increments and decrements, consistent with observations that motion responses can be evoked even when a sequential change in luminance at two points in space occurs with a delay period of up to 10 s in experiments using apparent motion stimuli<sup>3,19</sup>.

In HRC models, the individual inputs to the cells that perform the nonlinear amplification step are not themselves direction selective. We therefore tested the responses of Mi1, Tm3, Tm1 and Tm2 to motion stimuli, using light and dark bars moving in different directions, under conditions that evoke strong responses from lobula plate tangential cells<sup>20</sup> (Extended Data Fig. 3). All four neurons responded to moving bars with a sharp depolarization (Extended Data Fig. 3a, b) but the amplitude of these responses was independent of the direction of motion (Extended Data Fig. 3c). Thus, Mi1, Tm3, Tm1 and Tm2 are not direction selective under these conditions, consistent with these cells acting upstream of the nonlinear correlation stage of motion detection, as recently reported for Tm2 (ref. 18).

We next examined whether Mi1 and Tm3, or Tm1 and Tm2, have different response latencies that would allow them to differentially delay responses to contrast changes. To quantitatively capture the responses of these neurons to dynamic stimuli spanning a wide range of contrast values and time-scales, we used an approximately Gaussian-distributed random flicker stimulus with a 50% contrast (standard deviation) and an exponential correlation time of 10 ms (see Methods). We used standard procedures to extract the linear filter that best described the temporal properties of the response<sup>21,22</sup> (see Methods). The responses of Mi1 and Tm3 to the noise stimuli were very similar ( $r = 0.91$  between mean response traces), with temporal filters that comprised a large positive lobe reflecting a sign-conserving relationship between the contrast input and the neural response (Fig. 3a, b left (arrow) and Extended Data Figs 4a and 5a, b). Mean Tm1 and Tm2 responses to these noise stimuli were also similar to one another ( $r = 0.90$ ), with temporal filters that included a large negative lobe, reflecting a sign-inversion between the contrast input and the neural response (Fig. 3d, e left, arrow; Extended Data Figs 4b and 5e, g). For Mi1 the average peak response time was 71 ms after a contrast change (s.e.m. = 3.8 ms) while it was 53 ms (s.e.m. = 5.2 ms) for Tm3. Thus, a difference of 18 ms existed between the peak times of the filters for Mi1 and Tm3 (Fig. 3b right;  $P < 0.01$ ). Similarly, the average peak time was 56 ms (s.e.m. = 3.8 ms) for Tm1 and 43 ms (s.e.m. = 2.7 ms) for Tm2. The difference in latency between the two cells was 13 ms (Fig. 3e right;  $P < 0.002$ ). Thus, in both cases, there was a small but significant temporal offset, with Mi1 exhibiting a delayed response compared with Tm3, and Tm1 being delayed relative to Tm2. Notably, these peak delay differences are not much smaller than delays inferred from some lobula plate tangential cells recordings and behavioural experiments<sup>3,23,24</sup>.

We next asked whether neuronal responses to this stochastic stimulus were linear or whether different gains were applied to brightness increments and decrements. The noise stimulus was convolved with the corresponding filters for each neuron type to obtain the predicted linear response of each neuron. We then compared the linear predictions with the actual response to define the instantaneous nonlinearity for each neuron. Consistent with the light step results, the nonlinearities extracted for Mi1 and Tm3 revealed that these cells respond more strongly to brightness increments than to decrements (Fig. 3c and Extended Data Fig. 5b, d).

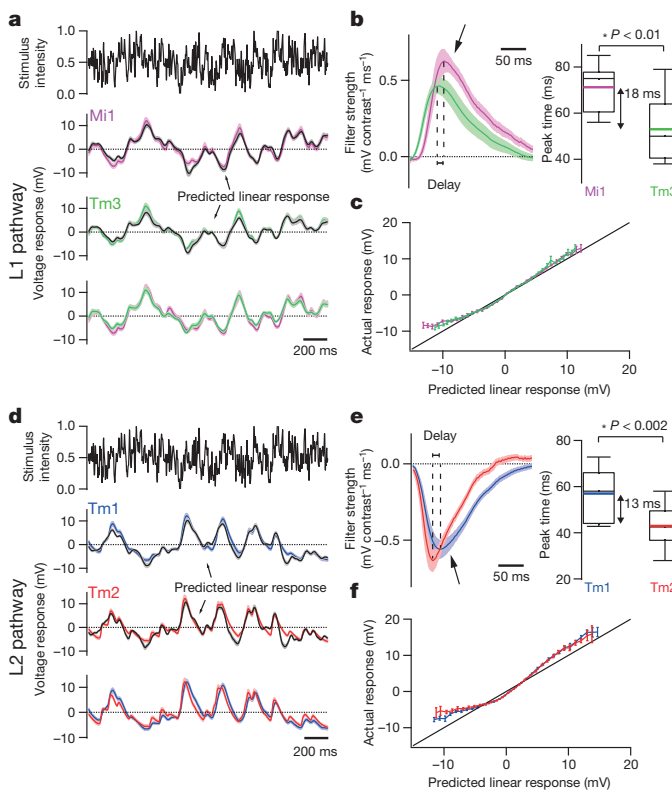


**Figure 3 | Mi1/Tm3 and Tm1/Tm2 respond with different delays and nonlinearities to a Gaussian noise stimulus.** **a**, Top: 2 s excerpt of the intensity signal from a 10 s full-field Gaussian noise stimulus. Signal correlation time was 10 ms (see Methods). Middle: average voltage response ( $\pm$  s.e.m.) of Mi1 ( $n = 7$ ) and Tm3 ( $n = 11$ ) to the 2 s noise stimulus on top. The black trace corresponds to the average predicted linear response ( $\pm$  s.e.m.) obtained by convolving the stimulus with the filters in **b**. Bottom: overlay of the Mi1 and Tm3 responses showing the high similarity in their response. **b**, Left: average linear filters extracted from the data in **a** that best predict the measured response of Mi1 and Tm3 as a function of preceding light intensity changes ( $\pm$  s.e.m.). The filters comprise a large positive lobe (arrow) and shallow negative lobe (see Extended Data Fig. 5). Right: box plots of the distribution of the timing of the peak responses of the Mi1 and Tm3 neurons. There is, on average, an 18 ms delay between the peak of Mi1 filters and Tm3 filters. Black line is the median, coloured line is the average. **c**, Average actual responses of Mi1 and Tm3 plotted against their average linear predicted responses. Error bars, s.e.m. A line of slope 1 is shown in black. **d–f**, Same as above for Tm1 ( $n = 15$ ) and Tm2 ( $n = 14$ ). The filters comprise a large negative lobe (arrow) and a shallow positive lobe (Extended Data Fig. 5). The average peak delay between the peak of Tm1 and Tm2 filters is 13 ms.

Similarly, both Tm1 and Tm2 neurons were less hyperpolarized in response to brightness increments and more depolarized in response to brightness decrements than predicted by the linear model (Fig. 3f and Extended Data Fig. 5f, h). The noise stimuli evoked smaller response asymmetries than those observed with brightness steps, possibly because these stimuli use smaller changes in intensity than our step stimuli. Such differences in gain for brightness increments and decrements reflect partial half-wave rectification, a central feature of models that selectively respond to one contrast polarity<sup>2,3,19,25</sup>.

Can the dynamics of the linear filters and the extent of the nonlinearities we measured account for well-characterized properties of motion detecting pathways? One hallmark of the HRC is that it displays a peak response to a defined temporal frequency, creating a temporal frequency optimum. Because of its structure, the output of an HRC is not proportional to the speed of motion, but rather increases to a maximum value, before decaying at faster speeds. The shape of this tuning curve depends on the temporal properties of its two input channels<sup>26</sup>. We constructed two separate model correlators, one that used Mi1 and Tm3 filters and

nonlinearities as the two channels preceding multiplication and subtraction, and a second one that used Tm1 and Tm2 filters and nonlinearities (Fig. 4a and data from Extended Data Fig. 6). We examined whether these model motion detectors produced temporal frequency tuning curves similar to those previously measured in flies. When we presented these models with moving sine waves of 20% contrast at various contrast frequencies, we observed a peak response at approximately 1 Hz for both the Mi1/Tm3 and the Tm1/Tm2 models (Fig. 4b). This computed temporal frequency optimum compares favourably with the optima measured in blowflies and *Drosophila*<sup>14</sup>.

Another measured feature of these two motion pathways is their selectivity for edges of particular contrast polarity. We presented our model correlators with light and dark edges of 100% contrast, moving across a grey background. The Tm1/Tm2 model was highly selective for dark edges over a range of speeds. The Mi1/Tm3 model was only mildly selective for light edges, owing to the more linear responses measured in Mi1 and Tm3 compared with Tm1 and Tm2 (Fig. 4c). These modelling results are consistent with experimentally measured high selectivity of the dark edge motion pathway<sup>2,3</sup>, and a more modest selectivity of the light edge motion pathway<sup>3</sup>.

Taken together, our data are consistent with a model in which Mi1 and Tm3 represent central components of the input channels of a correlator detecting moving light edges, while Tm1 and Tm2 represent analogous components for a correlator that is tuned to detect moving dark edges. The asymmetric responses of these four neurons to brightness increments and decrements corroborates previous studies that argued for separate processing of ON and OFF inputs by distinct channels<sup>15,25</sup>.

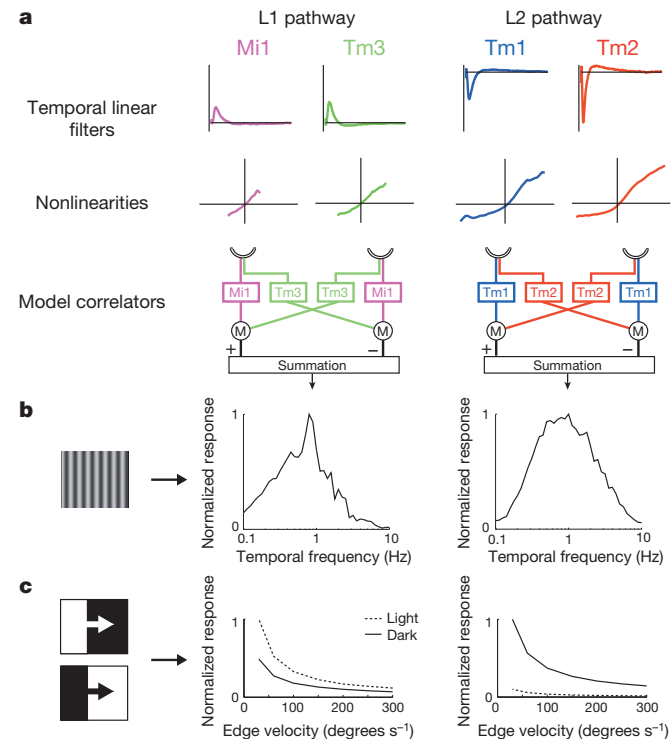


**Figure 4 | Modelling Mi1/Tm3 and Tm1/Tm2 as the delayed and non-delayed channels of light edges and dark edges correlators.** **a**, Left: the average filters and nonlinearities from the receptive field stochastic data set (200 s noise presentation, 50 ms correlation time, Extended Data Fig. 6) were used to model Mi1 and Tm3 as the delayed and non-delayed channels of a correlator model in bottom left. Right: same as left with Tm1 and Tm2 as the delayed and non-delayed channels of correlator model. **b**, Computed normalized temporal frequency tuning curves obtained numerically for the Mi1/Tm3 model correlator (left) and the Tm1/Tm2 model correlator (right) using sine waves of different temporal frequencies. **c**, Computed normalized response of the Mi1/Tm3 model correlator (left) and the Tm1/Tm2 model correlator (right) to light or dark edges of 100% contrast, moving at a range of speeds.

to explain the segregation between light and dark edge processing. This situation is similar to separate processing of ON and OFF signals by bipolar cells in the vertebrate retina<sup>27</sup>.

The relative delays we measured between the peak responses in these cells is roughly ten times smaller than previously calculated for idealized motion detector models that fit a host of experimental data. In classic HRC models, input to one channel is not filtered, while input to the second channel is low-pass filtered with a time constant of  $\tau$ . In these models, the maximum response occurs at a temporal frequency of  $1/2\pi\tau$ , so that the delay for a 1 Hz optimum is  $\tau \sim 150$  ms<sup>26</sup>. However, since both filters we measured act as band-pass filters, they suppress high-frequency inputs, while still producing delay differences between the channels. Thus, when input channels contain both these measured filters, a peak timing difference of  $\sim 15$  ms can result in a temporal frequency optimum of 1 Hz (see Methods and Extended Data Fig. 7). Furthermore, two considerations might lengthen the actual relative delays between pathways. First, we performed somatic recordings that may only approximate the true axonal response of the neurons. Second, the synapses between Mi1/Tm3 and T4, and those between Tm1/Tm2 and T5 could impose additional delays to either input channel before a correlation operation.

Anatomical reconstruction of the *Drosophila* medulla connected the predicted spatial receptive fields of Mi1 and Tm3 cells to the dendritic arbors of individual T4 cells with known directional preferences<sup>16</sup>. According to predictions derived from that analysis, if Mi1 signals are delayed relative to those of Tm3, as our recordings indicate, the observed direction selectivity in T4 could be accomplished by combining Mi1 and Tm3 inputs with opposite signs onto T4 (one inhibitory and the other excitatory). Such an arrangement could be similar to the motion detection model proposed to explain direction selective responses in the vertebrate retina<sup>16,28</sup>.

Given the cellular and synaptic complexity of medulla circuitry, as well as the wealth of distinct behaviours that are guided by visual motion, additional cell types are likely to play computational roles in *Drosophila* elementary motion detectors. Nonetheless, our data show that Mi1, Tm3, Tm1 and Tm2 possess response properties that are consistent with implementing the algorithmic steps that precede the correlation operations in the motion detecting pathways in *Drosophila*.

## METHODS SUMMARY

Green fluorescent protein (GFP)-targeted recordings were performed as described previously<sup>29</sup> under visual control using an Olympus microscope and a  $\times 60$  objective. Electrophysiology data were collected using Igor (Wavemetrics) running mafPC (courtesy of M. A. Xu-Friedman).

The drivers 686b-Gal4 and Bsh-Gal4 were used to target Mi1 neurons, R13E12-Gal4 for Tm3, 27b-Gal4 for Tm1, otd-Gal4 for Tm2 (see Methods for details about Gal4 driver lines). A cytosolic variant of UAS-GFP (a gift from G. Turner) was expressed under the control of the drivers to visualize the neurons.

Visual stimulation used a digital light projector coupled to a coherent fibre optic bundle to project images on a screen as described previously<sup>3</sup>.

Data were analysed using custom-written Matlab code. Filter extraction used standard methods<sup>22</sup>.

**Online Content** Methods, along with any additional Extended Data display items and Source Data, are available in the online version of the paper; references unique to these sections appear only in the online paper.

Received 17 November 2013; accepted 1 May 2014.

Published online 6 July 2014.

- Hassenstein, V. & Reichardt, W. System theoretical analysis of time, sequence and sign analysis of the motion perception of the snout-beetle *Chlorophanus*. *Z. Naturforsch. B* **11**, 513–524 (1956).
- Joesch, M., Schnell, B., Raghu, S. V., Reiff, D. F. & Borst, A. ON and OFF pathways in *Drosophila* motion vision. *Nature* **468**, 300–304 (2010).
- Clark, D. A., Bursztein, L., Horowitz, M. A., Schnitzer, M. J. & Clandinin, T. R. Defining the computational structure of the motion detector in *Drosophila*. *Neuron* **70**, 1165–1177 (2011).

- Borst, A. & Egelhaaf, M. Principles of visual motion detection. *Trends Neurosci.* **12**, 297–306 (1989).
- Buchner, E. Elementary movement detectors in an insect visual system. *Biol. Cybern.* **24**, 85–101 (1976).
- Meinertzhagen, I. & O’Neil, S. Synaptic organization of columnar elements in the lamina of the wild type in *Drosophila melanogaster*. *J. Comp. Neuro.* **305**, 232–263 (1991).
- Rister, J. *et al.* Dissection of the peripheral motion channel in the visual system of *Drosophila melanogaster*. *Neuron* **56**, 155–170 (2007).
- Katsov, A. Y. & Clandinin, T. R. Motion processing streams in *Drosophila* are behaviorally specialized. *Neuron* **59**, 322–335 (2008).
- Tuthill, J. C., Nern, A., Holtz, S. L., Rubin, G. M. & Reiser, M. B. Contributions of the 12 neuron classes in the fly lamina to motion vision. *Neuron* **79**, 128–140 (2013).
- Silkes, M. *et al.* Modular use of peripheral input channels tunes motion-detecting circuitry. *Neuron* **79**, 111–127 (2013).
- Bausenwein, B., Dittrich, A. & Fischbach, K.-F. The optic lobe of *Drosophila melanogaster*. *Cell Tissue Res.* **267**, 17–28 (1992).
- Maisak, M. S. *et al.* A directional tuning map of *Drosophila* elementary motion detectors. *Nature* **500**, 212–216 (2013).
- Schnell, B., Raghu, S. V., Nern, A. & Borst, A. Columnar cells necessary for motion responses of wide-field visual interneurons in *Drosophila*. *J. Comp. Physiol. A* **198**, 389–395 (2012).
- Borst, A., Haag, J. & Reiff, D. F. Fly motion vision. *Annu. Rev. Neurosci.* **33**, 49–70 (2010).
- Bausenwein, B. & Fischbach, K.-F. Activity labeling patterns in the medulla of *Drosophila melanogaster* caused by motion stimuli. *Cell Tissue Res.* **270**, 25–35 (1992).
- Takemura, S.-y. *et al.* A visual motion detection circuit suggested by *Drosophila* connectomics. *Nature* **500**, 175–181 (2013).
- Shinomiya, K. *et al.* Candidate neural substrates for off-edge motion detection in *Drosophila*. *Curr. Biol.* **24**, 1–9 (2014).
- Meier, M. *et al.* Neural circuit components of the *Drosophila* OFF motion vision pathway. *Current Biol.* (2014).
- Eichner, H., Joesch, M., Schnell, B., Reiff, D. F. & Borst, A. Internal structure of the fly elementary motion detector. *Neuron* **70**, 1155–1164 (2011).
- Joesch, M., Plett, J., Borst, A. & Reiff, D. F. Response properties of motion-sensitive visual interneurons in the lobula plate of *Drosophila melanogaster*. *Curr. Biol.* **18**, 368–374 (2008).
- Chichilinsky, E. J. A simple white noise analysis of neuronal light responses. *Network* **12**, 199–213 (2001).
- Baccus, S. A. & Meister, M. Fast and slow contrast adaptation in retinal circuitry. *Neuron* **36**, 909–919 (2002).
- Harris, R. A., O’Carroll, D. C. & Laughlin, S. B. Contrast gain reduction in fly motion adaptation. *Neuron* **28**, 595–606 (2000).
- Marmarelis, P. Z. & McCann, G. D. Development and application of white-noise modeling techniques for studies of insect visual nervous system. *Kybernetik* **12**, 74–89 (1973).
- Franceschini, N., Riehle, A. & Le Nestour, A. in *Facets of Vision* (eds Stavenga, D. G. & Hardie, R. C.) Ch. 17, 360–390 (Springer, 1989).
- Borst, A. & Bahde, S. What kind of movement detector is triggering the landing response of the housefly? *Biol. Cybern.* **55**, 59–69 (1986).
- Wässle, H. Parallel processing in the mammalian retina. *Nature Rev. Neurosci.* **5**, 747–757 (2004).
- Barlow, H. & Levick, W. R. The mechanism of directionally selective units in rabbit’s retina. *J. Physiol. (Lond.)* **178**, 477–504 (1965).
- Wilson, R. I., Turner, G. C. & Laurent, G. Transformation of olfactory representations in the *Drosophila* antennal lobe. *Science* **303**, 366–370 (2004).
- Fischbach, K.-F. & Dittrich, A. The optic lobe of *Drosophila melanogaster*. I. A Golgi analysis of wild-type structure. *Cell Tissue Res.* **258**, 441–475 (1989).

**Acknowledgements** We thank G. Turner for his initial help on whole-cell recordings; X. Li for providing the confocal image of the 686-Gal4 flip-out clone, and N. Vogt, J. Rister and members of the Clandinin laboratory, as well as H. S. Seung and S. A. Baccus, for reading of the manuscript. We also thank D. B. Chklovskii for suggesting recording from Tm3 and T. Erclik for identifying the Tm3 Gal4 line. This work was supported by a grant from the National Institutes of Health (NIH) (R01EY017916) and a grant from New York University Abu Dhabi Institute (G1205C) to C.D.; R.B. was supported by fellowships from EMBO and the Human Frontier Science Program. This work was also supported by grants from the NIH to T.R.C. (R01EY022638 and DP1 OD003530). D.A.C. was partly supported by an NIH T32 Vision Training Grant and a Jane Coffin Childs postdoctoral fellowship. A.G.C. was supported by a Scholar Award from The McKnight Foundation.

**Author Contributions** R.B. designed experiments, performed electrophysiological recordings and analysed the data. D.A.C. designed visual stimuli and experiments, analysed the data and performed modelling. A.G.C. provided electrophysiological training and advice to R.B. T.R.C. and C.D. contributed to the design of experiments. R.B., D.A.C., T.R.C. and C.D. wrote the manuscript.

**Author Information** Reprints and permissions information is available at [www.nature.com/reprints/](http://www.nature.com/reprints/). The authors declare no competing financial interests. Readers are welcome to comment on the online version of the paper. Correspondence and requests for materials should be addressed to R.B. (rb141@nyu.edu) or D.A.C. (damon.clark@yale.edu).

## METHODS

**Flies.** Flies were reared on standard molasses-based medium at 25 °C. Flies used for electrophysiology were of the following genotype: *w<sup>+</sup>*; *UAS-cytosolicGFP/UAS-cytosolicGFP*; *686-Gal4/+* or *TM2* (Extended Data Fig. 8a, also labels Tm2 in the medulla) or *w<sup>+</sup>*; *UAS-cytosolicGFP/UAS-cytosolicGFP*; *Bsh-Gal4/+* or *TM2* for Mi1<sup>31</sup> (also labels L4 and L5 in the lamina), *w<sup>+</sup>*; *UAS-cytosolicGFP/UAS-cytosolicGFP*; *R13E12-Gal4/+* or *TM2* from the Janelia Farms Gal4 collection<sup>32</sup> for Tm3 (Extended Data Fig. 8a, also labels unidentified medulla tangential cells), *w<sup>+</sup>*; *UAS-cytosolicGFP/UAS-cytosolicGFP*; *27b-Gal4/+* or *TM2* for Tm1 (ref. 33) (also labels Pm1 and Pm2 in the medulla), *w<sup>+</sup>*; *UAS-cytosolicGFP/UAS-cytosolicGFP*; *otd-Gal4/+* or *TM2* for Tm2 (ref. 33) (also labels photoreceptors). All experimental animals were briefly anaesthetized using carbon dioxide within 1 to 2 days of eclosion, and tested at least 3 h later at room temperature.

**Electrophysiology.** Flies were prepared for *in vivo* whole-cell patch-clamp recording using the following procedure, based on ref. 34. The flies were immobilized in a perforated piece of foil. A window was cut in the caudal backside of the head at the edge of the retina to expose the cell bodies of medulla cortex neurons. The eyes and the ventral side of the fly were facing down under the foil, which separates the upper part of the preparation covered with saline, from the lower dry part. The saline composition was as follows (in mM): 103 NaCl, 3 KCl, 5 N-tris(hydroxymethyl) methyl-2-aminoethane-sulphonic acid, 8 trehalose, 10 glucose, 26 NaHCO<sub>3</sub>, 1 NaH<sub>2</sub>PO<sub>4</sub>, 1.5 CaCl<sub>2</sub>, and 4 MgCl<sub>2</sub>, adjusted to 270 mOsm. The pH of the saline equilibrated near 7.3 when bubbled with 95% O<sub>2</sub>/5% CO<sub>2</sub> and perfused continuously over the preparation at 2 ml min<sup>-1</sup>. Patch-clamp electrodes (resistance 6–12 MΩ) were pressure polished and filled with a solution composed of the following (in mM): 125 potassium aspartate, 10 HEPES, 1 KCl, 4 MgATP, 0.5 Na<sub>3</sub>GTP, and 1 EGTA, 13 biocytin hydrazide, pH 7.3, adjusted to 265 mOsm. In most cells, it was necessary to inject a small constant hyperpolarizing current immediately after break-in (0–5 pA), to bring the membrane potential close to -60 mV, which had no effects on the character of light responses while the potential was in the range -50 to -60 mV, spanning the likely range of physiological resting potentials.

The membrane potential was measured in current-clamp mode using a Multiclamp 700B amplifier (Axon). Electrophysiology data were collected using Igor Pro (WaveMetrics) running mafPC (courtesy of M. A. Xu-Friedman). The analysis used Igor Pro and Matlab.

Recordings were obtained under visual control using an Olympus BX51 with ×60 water-immersion objective. The preparation was visualized using transmitted infrared illumination and a long-pass filter (850 nm). The contrast was adjusted on the camera to visualize the shape of the neurons. Neurons of interest were marked using a cytosolic variant of GFP, and the fluorescence excitation was briefly turned on before patching for identification. One neuron was recorded per fly. Recordings were discarded if large changes in input resistance or resting potential were detected.

Two distinct classes of Mi1 responses were found (Fig. 2a and Extended Data Fig. 9). In one class, detailed in the results, responses to steps were transient (Fig. 2). The second class (65% of recorded Mi1 neurons) comprised cells that depolarized in response to brightness increments, but responded tonically (that is, persistently) during light presentation and returned to pre-step levels only when the light was turned off (Extended Data Fig. 9a, b). These Mi1 neurons depolarized fully in response to very small increases in light and, given their elevated membrane potential, could not respond strongly to further brightness increments (Extended Data Fig. 9b). In some instances, cells switched from the transient class to this tonic class over a few minutes, and remained tonic thereafter. The converse switch from tonic to transient was never observed. A similar phenomenon was also observed in a small fraction of Tm3 neurons (18%). For these reasons we believe that the tonic neuronal measurements are non-physiological, and have excluded those neurons' responses from all subsequent analyses.

**Visual stimulation.** Visual stimulation was performed as described previously<sup>3,35</sup>. Grey-scale images were projected onto a screen using a digital light projector (Infocus DepthQ) coupled with a coherent fibre optic (100 fibres per millimetre, 0.63 numerical aperture) (Schott) and a lens. The screen was 55 mm × 55 mm, placed 40 mm away from the fly. Visual stimuli were created using custom-written code in Matlab, using PsychToolBox<sup>36</sup>. The mean radiance was 1.1 W sr<sup>-1</sup> m<sup>-2</sup>, which corresponds to ~250 cd m<sup>-2</sup>, and the stimulus was updated at 240 Hz, by using colour channels as independent intensity channels with the colour wheel removed<sup>3</sup>.

The random flicker stimuli were presented on a background luminance, so that the intensity  $q(t) = m(1 + s(t))$ , where  $m$  is the mean background luminance and  $s(t)$  is constructed to be Gaussian distributed with zero mean and standard deviation  $\sigma$ . The timelag autocovariance of  $s(t)$  was constructed to be  $C_{ss}(t) = \sigma^2 e^{-|t|/\tau}$ , where  $\tau$  is the reported correlation time for the input and  $\sigma$  is the reported contrast. The intensity  $q(t)$  was bounded below by 0 and above by  $2m$ , so that the distribution was approximately Gaussian and rarely clipped when contrast was 50% or below. Slower correlation times put more power into low frequencies, which were less attenuated by low-pass filter properties of the system. Our filter extraction method

(see below) accounts for these stimulus correlations when computing the empirical linear filters. Qualitatively, the response of each of the four cell types to this stimulus was robust and highly reproducible, with no systematic differences observed across identical presentations of the same stimulus (Extended Data Fig. 4a, b).

**Filters and nonlinearities.** Linear filters were extracted using methods described in ref. 22. Before extracting filters, membrane voltage measurements were filtered with a 60 Hz notch filter to exclude noise in that frequency, and with a high-pass filter with cutoff frequency of 0.008 Hz. Briefly, the filter estimate,  $\hat{K}(\omega)$ , for a stimulus,  $s(t)$ , and response,  $r(t)$ , was computed in Fourier space to be

$$\hat{K}(\omega) = \frac{\hat{C}_{rs}(\omega)}{\hat{C}_{ss}(\omega)}$$

where the numerator is the covariance between stimulus and response and the denominator is the autocovariance of the stimulus. These two functions were estimated by computing

$$\hat{C}_{rs}(\omega) = \langle \tilde{r}(\omega)\tilde{s}^*(\omega) \rangle$$

$$\hat{C}_{ss}(\omega) = \langle \tilde{s}(\omega)\tilde{s}^*(\omega) \rangle$$

where  $\tilde{r}(\omega)$  and  $\tilde{s}(\omega)$  are the Fourier transforms of  $r(t)$  and  $s(t)$ . The averages in each case are performed over 5-s-long snippets of stimulus and response traces, taken every 0.1 s over the entire trace. The snippets were zero-padded before the fast Fourier transform. To prevent the amplification of high frequencies in the filter, the quotient was regularized by adding to  $\hat{C}_{ss}(\omega)$  a small term equal to 1% of the average value of  $\hat{C}_{ss}(\omega)$  over all frequencies. Lengthening the snippet duration, eliminating the zero-padding and using a non-Fourier-transformed estimate of the filter<sup>19</sup> all yielded filters with shapes and peak locations almost indistinguishable from this method. The filters shown in the figures are the inverse Fourier transforms of the filters  $\hat{K}(\omega)$  computed for each neuron.

Instantaneous ('static') nonlinearities were obtained by plotting actual responses against linear predictions. The linear predictions were binned and the mean actual response was computed for each bin. This operation was performed across cells, and then averaged by bin to obtain the mean and s.e.m. values of the nonlinearity.

In addition to the filter relating output to input, we also computed the coherence between input and output for all four neurons, shown in Extended Data Fig. 4c. The coherence,  $\gamma^2$ , was computed as

$$\gamma^2 = \frac{|\hat{C}_{rr}(\omega)|^2}{\hat{C}_{ss}(\omega)\hat{C}_{rr}(\omega)}$$

where  $\hat{C}_{ss}(\omega)$  and  $\hat{C}_{rs}(\omega)$  were computed as before, and  $\hat{C}_{rr}(\omega) = \langle \tilde{r}(\omega)\tilde{r}^*(\omega) \rangle$ . Regularization was unnecessary, since coherence is bounded above by 1. Deviations of the coherence from 1 show the influence of nonlinearities in the input-output relationship or the influence of noise in the response.

**Statistics.** Sample sizes were commensurate with other studies in the field. All statistical tests were two-tailed Student's *t*-tests. Some results are presented using Pearson correlation coefficients (*r* values). We did not test for normality of distributions.

**Modelling.** To model the responses of the four interneurons, we gathered a distinct set of data to sample a range of lower frequencies. Indeed, the full-field presentations of the noise stimulus in Fig. 3 were 10 s long, which did not provide many instances of low-frequency stimuli that could be used to fit a filter. To generate the new stimuli and responses, we displayed a grid of 256 squares to flies (each square was approximately 5° across, depending on position on the screen), with each square displaying a Gaussian noise stimulus with a correlation time of 50 ms. The entire stimulus in this case lasted 200 s, so that low-frequency stimuli were sampled better than in the 10 s presentations. The temporal filters and nonlinearities obtained with this stimulus were similar to those computed with the full-field noise stimulus, but the longer stimulus allowed a higher-quality estimate at longer times (Extended Data Fig. 6).

Examples of receptive fields obtained with this method are presented in Extended Data Fig. 6a. In these experiments, we chose the strongest pixels, whose filter amplitudes were 3.7 or more standard deviations from the mean ( $P < 0.05$ , Bonferroni-corrected for the number of squares), and summed them to obtain a filter for each cell. Instantaneous nonlinearities in these experiments were computed by comparing the actual response to the sum of the predicted responses due to these pixels.

Using this data set, we created two models to test hypotheses about the filters and nonlinearities we measured in these four neurons. The first was a detailed model, in which we incorporated as many measurements and known quantities as possible. We used this model to compare predictions from our data to two prominent measurements in the literature. The second model was a toy model, which was entirely linear in its filtering and could include far simpler filters than the empirical ones. We used the toy model to gain insight into how filter combinations with small timing

differences could generate peak stimulus responses at relatively low temporal frequencies. All modelling used custom-written code in Matlab (Mathworks).

**Detailed model.** Our detailed model used the linear filters and instantaneous nonlinearities shown in Fig. 4, extracted from the long stimulus presentation (Extended Data Fig. 6). Two photoreceptors, *a* and *b*, with Gaussian angular acceptance functions and spacing  $\Delta\phi$ , equal to  $5.1^\circ$ , served as inputs to our motion detector. The spatial filter was

$$g(\theta) = \frac{1}{Z} e^{-\frac{\theta^2}{2q^2}}$$

where  $Z$  is chosen to normalize the function,  $\theta$  is azimuthal angle and  $q$  was chosen to match the measured value of full width at half maximum of  $5.7^\circ$  (ref. 37). The photoreceptor spatial receptive fields were centred on  $\theta_a$  and  $\theta_b$ , so that  $\Delta\phi = \phi_b - \phi_a$ . Thus, from a space–time contrast input  $S(\theta, t)$  (similar to our  $s(t)$  above, but also a function of azimuthal angle  $\theta$ ), two signals emerged from the model photoreceptors:

$$s_a(t) = \int d\theta' S(\theta', t) g(\theta' - \theta_a)$$

$$s_b(t) = \int d\theta' S(\theta', t) g(\theta' - \theta_b)$$

These two signals were each filtered by two empirical temporal filters,  $f_1(t)$  and  $f_2(t)$ , where the pairing was Tm2-and-Tm1 or Tm3-and-Mi1. After filtering, the signals were transformed by the empirical nonlinearities,  $N_1(\cdot)$  and  $N_2(\cdot)$ . Thus, the two signals originating at photoreceptor *a*, after filtering and including the nonlinearity, were

$$F_{ia}(t) = N_i \left( \int_{-\infty}^t dt' s_a(t') f_i(t-t') \right)$$

where  $F_{ia}(t)$  is the output of the linear–nonlinear model corresponding to filter *i* on the signal from photoreceptor *a*. Thus, with two photoreceptors and two filters, there were four total signals after filtering and including the static nonlinearities. To obtain the model output, we combined the signals in the antisymmetric fashion of the HRC<sup>1</sup>:

$$R(t) = (F_{2a}(t) \times F_{1b}(t)) - (F_{2b}(t) \times F_{1a}(t)) \quad (1)$$

where the subscripts 1 and 2 refer to filters and subscripts *a* and *b* refer to the photoreceptor position. This model was used to compute the mean responses in Fig. 4b. The responses in Fig. 4c are the integrated responses of this model to high-contrast light and dark edges moving over a grey background.

**Toy model.** In addition to the detailed models in Fig. 4 for Mi1/Tm3 and Tm1/Tm2, we constructed a second ‘toy model’. The aim of the toy model was to gain intuition for how a small difference in filter timescales could produce a relatively low temporal frequency optimum. This model is like the realistic one, except that the two spatial filters were represented by spatially separated delta functions, and no nonlinearities were applied before the multiplication step. In this case, it is possible to compute analytical results<sup>26</sup>. The classic equation for the steady-state HRC response to a moving sine wave grating of wavelength  $\lambda$ , contrast  $\Delta I$  and temporal frequency  $\omega$ , is:

$$R(\omega) = |\tilde{f}_1(\omega)| |\tilde{f}_2(\omega)| \sin(\Phi_1(\omega) - \Phi_2(\omega)) (\Delta I)^2 \sin(2\pi\Delta\phi/\lambda) \quad (2)$$

where  $\tilde{f}_1(\omega)$  and  $\tilde{f}_2(\omega)$  are the Fourier transforms of the filters for the two input arms to the correlator,  $\Phi_1(\omega)$  and  $\Phi_2(\omega)$  are the phase shift of each filter, and  $\Delta\phi$  is the angular separation between the two photoreceptor inputs.

Equation (2) gives the predicted response of an HRC to a sine wave of a given temporal frequency, and simplifies easily under certain circumstances. The first two terms give the amplitudes of the input sine waves after passing through the filters, while the phase term  $\sin(\Phi_1(\omega) - \Phi_2(\omega))$  relies on the different phases generated by the two filters, and is a result of the antisymmetric subtraction in the model. The last term is a geometrical term that relates the overall response amplitude to the wavelength of the sinewave input and the distance between photoreceptor receptive fields.

In Extended Data Fig. 7a, we plot the first three terms in equation (2) (normalizing the two filters by the maximum filter strengths,  $\max(|\tilde{f}_1(\omega)|)$  and  $\max(|\tilde{f}_2(\omega)|)$ ), and the relative total response. The relative total response is the product of the first three terms in equation (2) (with filters normalized as above), effectively setting  $(\Delta I)^2 \sin(2\pi\Delta\phi/\lambda) = 1$ . For the two model HRCs we compute both Tm3 + Mi1 and Tm2 + Tm1. The phase terms are 0.2–0.4 for these filter pairings in the region around 1 Hz. Much of the decrease in response at higher frequencies comes from the low-pass nature of the filters, rather than from the phase term. These analytical HRC responses agree closely with our numerical computations in Fig. 4 when the input amplitude is small, so that the nonlinearities do not greatly affect the numerical results.

If  $f_1(t) = \delta(t)$  and  $f_2(t) = \frac{1}{\tau} e^{-t/\tau}$ , then

$$R(\omega) \sim \frac{\omega\tau}{1 + \omega^2\tau^2}$$

which has a maximum value at  $\omega = 1/\tau$ , or a frequency of  $1/2\pi\tau$  cycles per second, which equals 1 Hz when  $\tau \sim 150$  ms. This is the origin of the 150 ms time constant often referred to in the literature<sup>23</sup>. Extended Data Fig. 7c shows the components of the HRC response for this model, with  $\tau = 150$  ms. The decrease in response at high frequency comes from the low-pass filter, while the decrease at low frequency comes from the phase term.

If the filters in the toy model are both first-order low-pass, so that  $f_1(t) = \frac{1}{\tau_1} e^{-t/\tau_1}$  and  $f_2(t) = \frac{1}{\tau_2} e^{-t/\tau_2}$ , then the steady-state response can also be worked out:

$$R(\omega) \sim \frac{\omega(\tau_2 - \tau_1)}{(1 + \omega^2\tau_1^2)(1 + \omega^2\tau_2^2)}$$

This simplifies to the previous result as one takes  $\tau_1 \rightarrow 0$ . The location of maximum response can be found numerically, or analytically with this solution:

$$\omega = \frac{1}{\sqrt{6}} \sqrt{\frac{\sqrt{\tau_1^4 + \tau_2^4 + 14\tau_1^2\tau_2^2} - 1}{\tau_1^2\tau_2^2} - \frac{1}{\tau_1^2} - \frac{1}{\tau_2^2}}$$

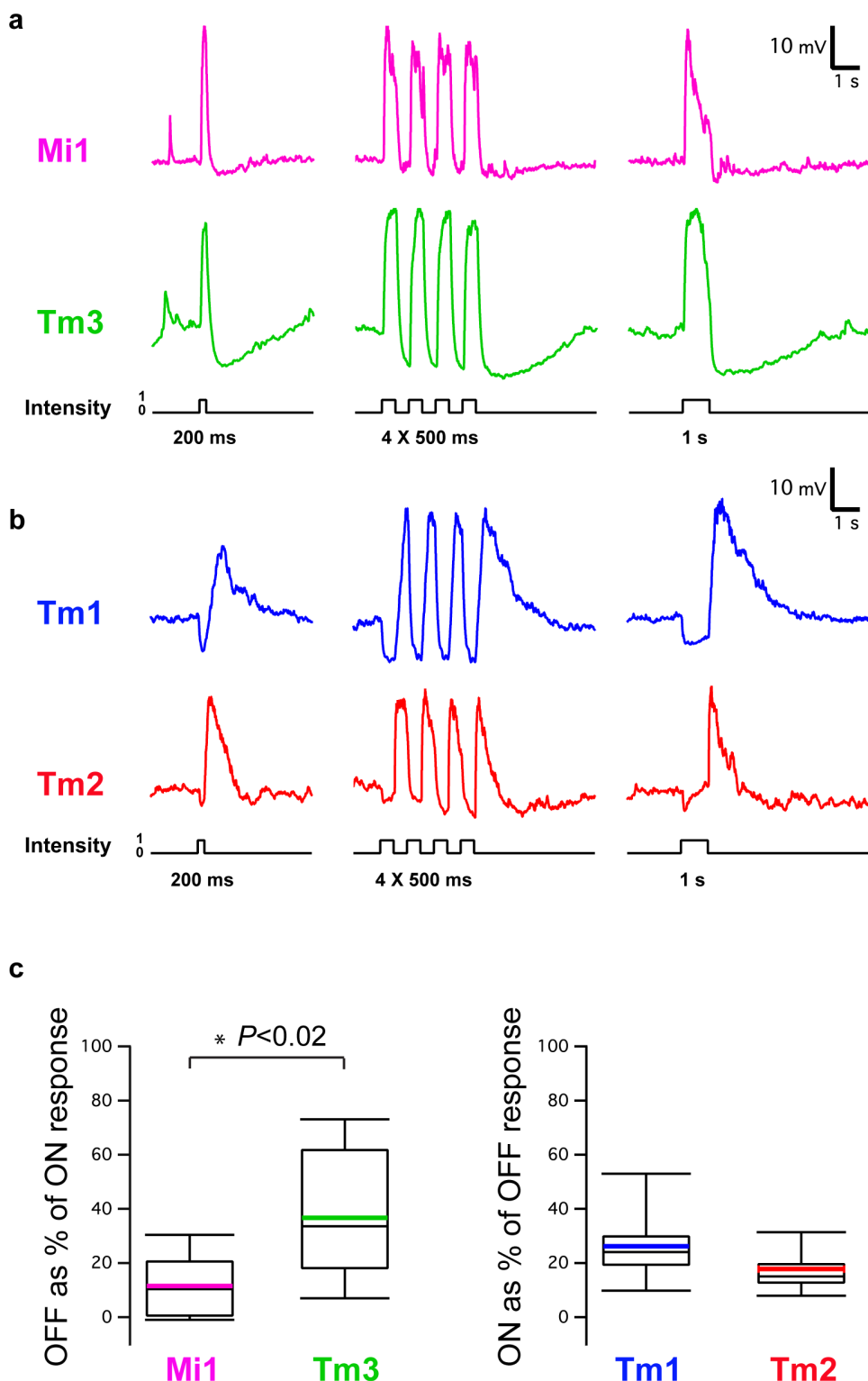
In Extended Data Fig. 7d, we plot the components of the HRC response in the case of two low-pass filters, with time constants of 40 and 55 ms, which roughly match the peak times we found in Tm2 and Tm1. This combination of filters gives a frequency optimum around 2 Hz, even though the difference in time constants is a factor of 10 smaller than the 150 ms found with the first model above. Note that these toy filters are pure low-pass filters, and look quite different from the biphasic filters we found empirically. The goal of this exercise was to gain intuition about simple filters on the two arms of an HRC.

In Extended Data Fig. 7E, we plot the contrast frequency optimum (in hertz) for various combinations of  $\tau_1$  and  $\tau_2$ . There are many combinations of these two filter values that result in contrast frequency optima in 1–3 Hz range. (When  $\tau_1$  and  $\tau_2$  invert order, so that  $\tau_1 < \tau_2$  becomes  $\tau_1 > \tau_2$ , the response inverts, so we locate the minimum of this inverted response.) When the two time-constants are very similar, the phase term in the response, along with the total response itself, becomes small (Extended Data Fig. 7f; again, when the order of  $\tau_1$  and  $\tau_2$  changes, we invert the response sign). In our normalized scaling, when the responses are small compared with 1, they may be susceptible to noise, since the signal is the difference between two signals from the multiplication steps, which can be much larger than their difference. Filter pairings with phase terms (and responses) that are closer to 1 are less susceptible to noise during the subtraction step of the HRC computation. In the empirical cases (Extended Data Fig. 7a, b), the phase terms and relative responses are larger than those in our toy model (Extended Data Fig. 7d) and closer to the toy model with very different low-pass filters (Extended Data Fig. 7c).

**Generation of clones.** The flies *hsFLP, FRT40A, UAS-CD8::GFP, UAS-rCD2-miRNA/CyO, y+* were crossed with *hsFLP, FRT40A, UAS-rCD2RFP, UAS-GFP-miRNA/CyO, y+* (gifts from T. Lee). The progeny larvae were heat-shocked at 37 °C for 12 min, and dissected as adults.

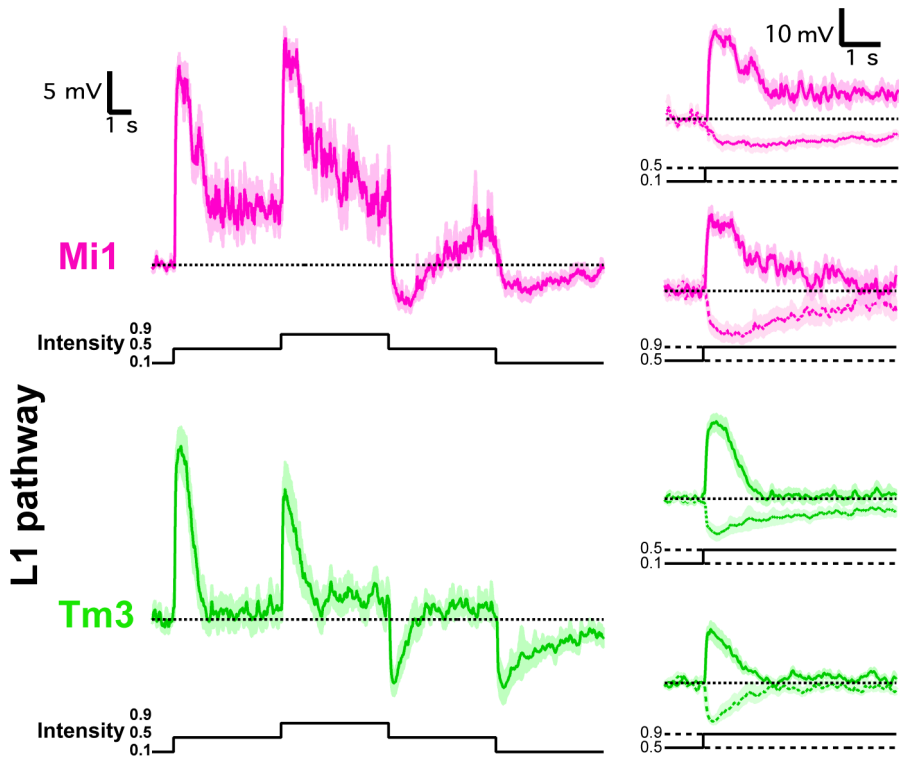
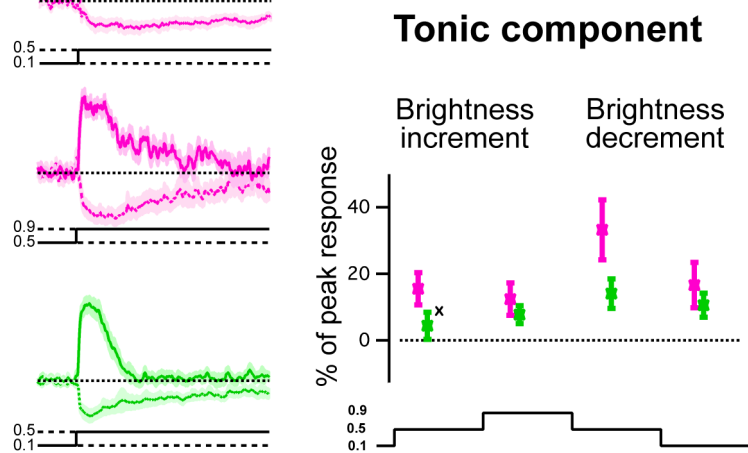
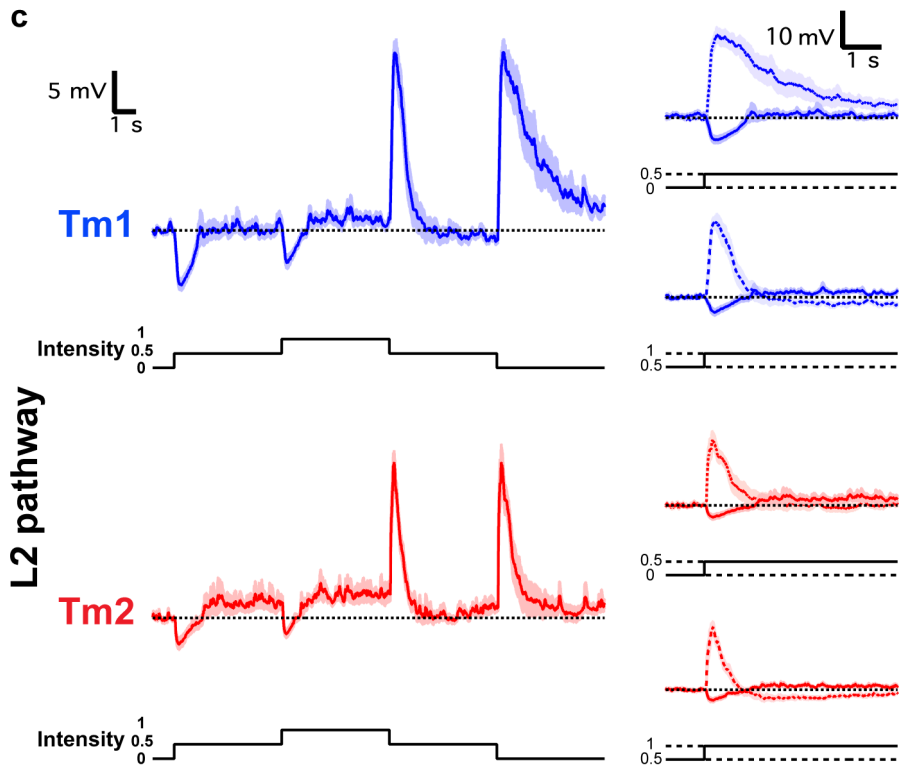
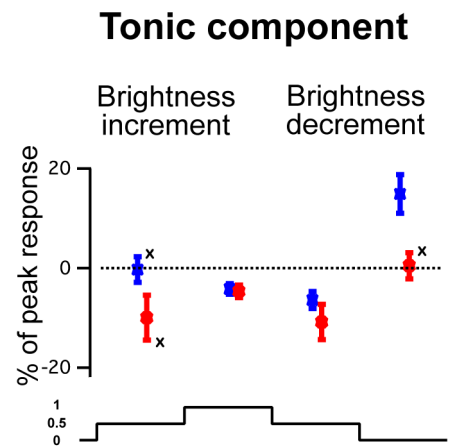
**Immunostaining.** These were done as described<sup>38</sup> with some modifications. Adult brains were dissected in 1× PBS, and fixed in 4% formaldehyde for 45 min on ice. Brains were incubated in primary antibody solution overnight at 4 °C and in secondary antibody solution at room temperature for 3 h. We used the following antibodies: sheep anti-GFP (1:500, AbD Serotec), rat anti-DN-cadherin (1:20, DSHB) and mouse anti-chaoptin (1/20, DSHB) diluted in 0.3% PBST (Triton X-100 in PBS). Images were acquired using a Leica SP5 confocal. Figures were assembled using Adobe Photoshop.

31. Hasegawa, E. et al. Concentric zones, cell migration and neuronal circuits in the *Drosophila* visual center. *Development* **138**, 983–993 (2011).
32. Jenett, A. et al. A GAL4-driver line resource for *Drosophila* neurobiology. *Cell Rep.* **2**, 991–1001 (2012).
33. Morante, J. & Desplan, C. The color-vision circuit in the medulla of *Drosophila*. *Curr. Biol.* **18**, 553–565 (2008).
34. Wilson, R. I. & Laurent, G. Role of GABAergic inhibition in shaping odor-evoked spatiotemporal patterns in the *Drosophila* antennal lobe. *J. Neurosci.* **25**, 9069–9079 (2005).
35. Freifeld, L., Clark, D. A., Schnitzer, M. J., Horowitz, M. A. & Clandinin, T. R. GABAergic lateral interactions tune the early stages of visual processing in *Drosophila*. *Neuron* **78**, 1075–1089 (2013).
36. Brainard, D. H. The psychophysics toolbox. *Spat. Vis.* **10**, 433–436 (1997).
37. Stavenga, D. Angular and spectral sensitivity of fly photoreceptors. II. Dependence on facet lens F-number and rhabdomere type in *Drosophila*. *J. Comp. Physiol. A* **189**, 189–202 (2003).
38. Morante, J. & Desplan, C. Dissection and staining of *Drosophila* optic lobes at different stages of development. *Cold Spring Harb. Protoc.* **2011**, 652–656 (2011).



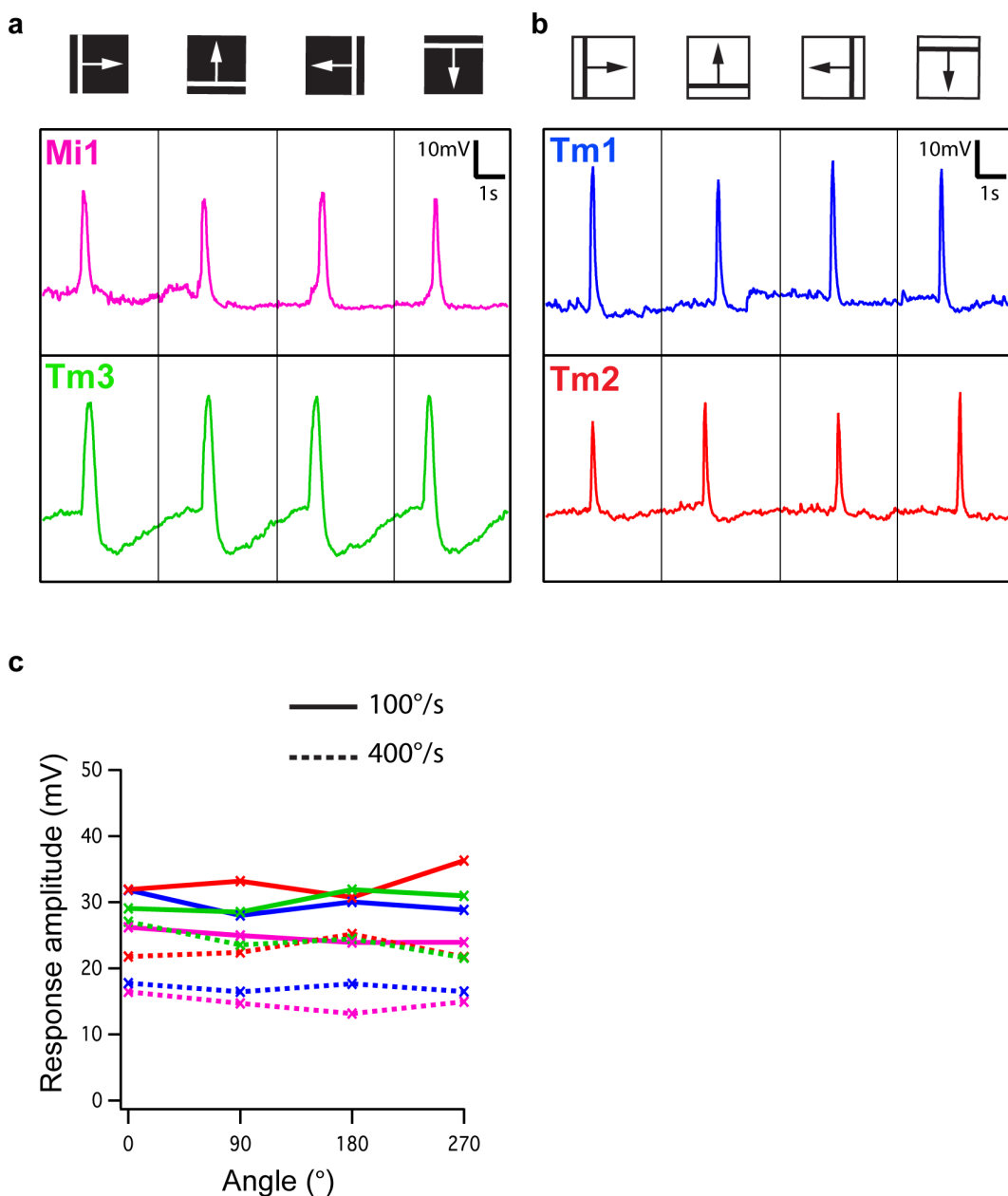
**Extended Data Figure 1 | Representative raw traces of responses to flashes of light of different duration from dark.** **a**, Top: response of an Mi1 neuron to 200 ms, four consecutive 250 ms and 1 s full-field flashes of light from dark. Bottom: same as top for a Tm3 neuron. **b**, Same as **a** for a Tm1 neuron and a

Tm2 neuron. **c**, Box plots illustrating the distribution of the OFF response as a percentage of the ON response for Mi1 ( $n = 7$ ) and Tm3 ( $n = 10$ ) and the ON response as a percentage of the OFF response for Tm1 ( $n = 10$ ) and Tm2 ( $n = 11$ ) averaged in Fig. 1. Black line, median; coloured line, average.

**a****b****c****d**

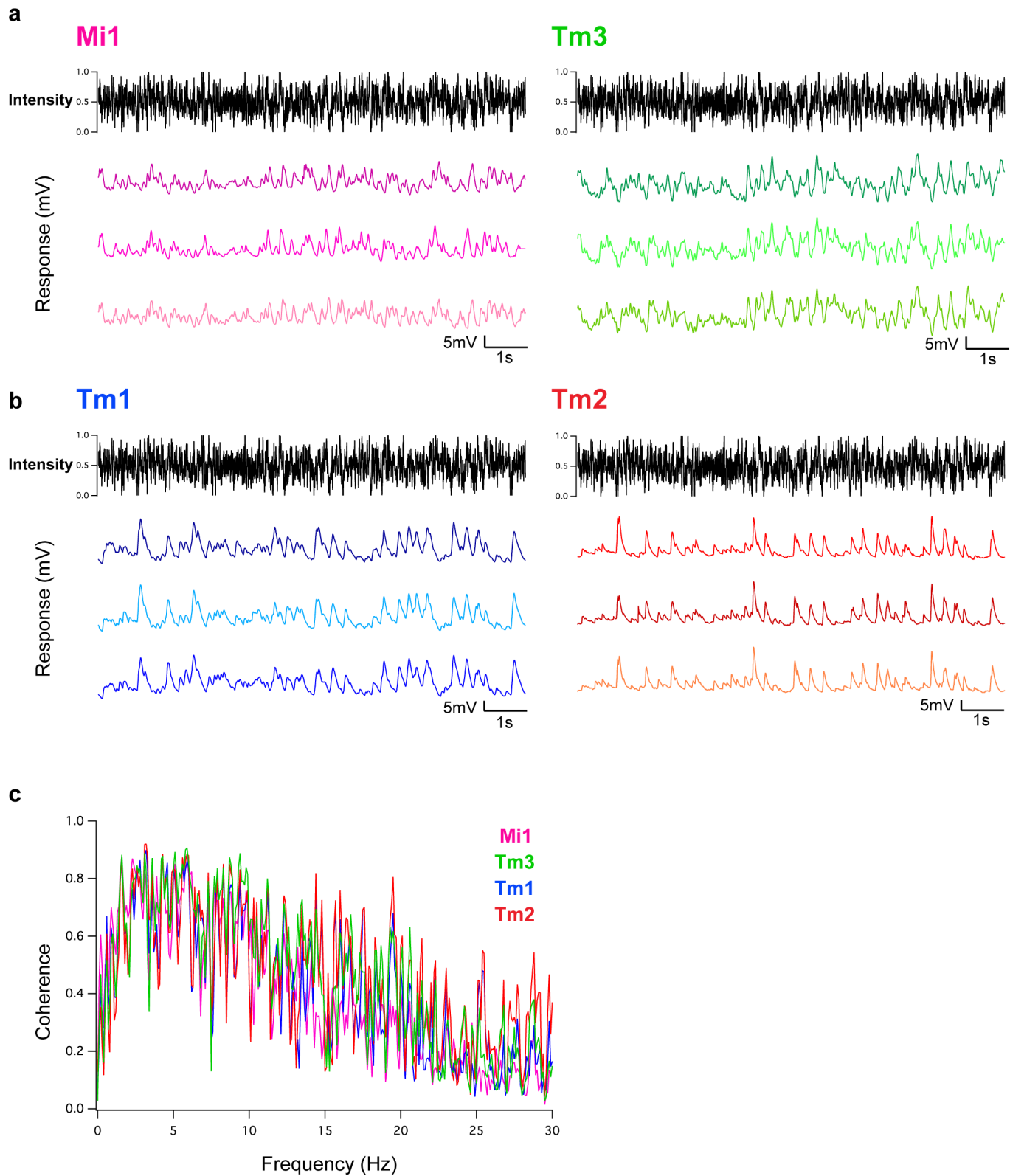
**Extended Data Figure 2 | Mi1, Tm3, Tm1 and Tm2 neurons encode stable information about luminance.** **a**, Top left: averaged evoked responses ( $\pm$  s.e.m.) of Mi1 ( $n = 7$ ) in response to 5 s steps of light from dark to grey (0.5 intensity) to light to grey to dark. Top right: excerpts from the left trace where the pre-contrast change voltages have been matched. Bottom left and right: same as above for Tm3 ( $n = 10$ ). **b**, Tonic component (average difference in membrane potential between post- and pre-contrast change between 4 and

5 s after contrast change) as a percentage of the maximum peak response for brightness increments of the corresponding contrast difference. Error bars, s.e.m. **c, d**, Same as **a** and **b** for Tm1 ( $n = 9$ ) and Tm2 ( $n = 7$ ). The tonic component was measured as a percentage of the peak response for brightness decrements of the corresponding contrast difference. In all cases, except for those marked with a cross, the distributions are significantly different from zero ( $P < 0.05$ ).



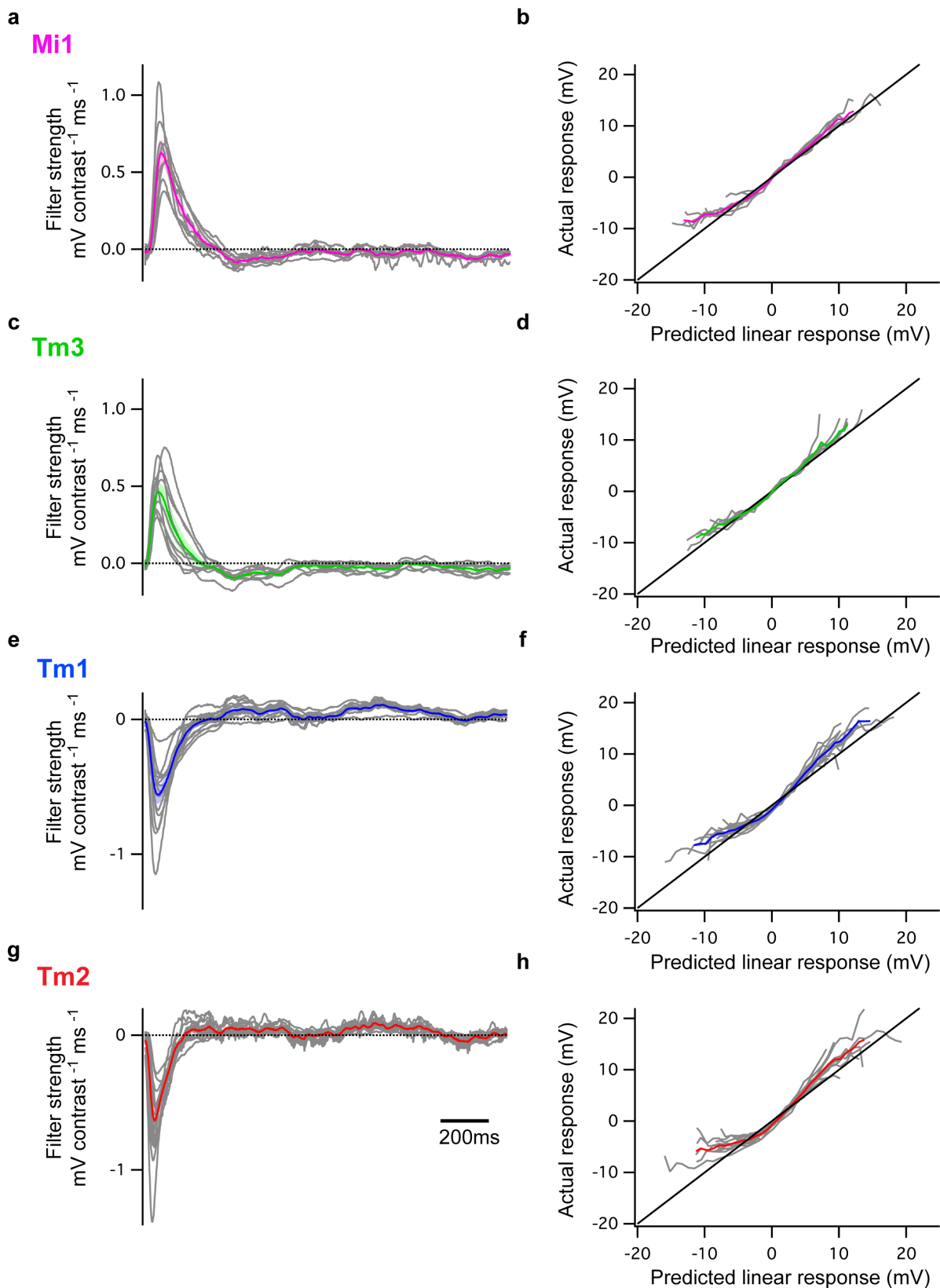
**Extended Data Figure 3 | Mi1, Tm3, Tm1 and Tm2 are not direction selective.** **a**, Top: response of an Mi1 neuron to a white bar moving rightwards, upwards, leftwards and downwards at  $100^{\circ} \text{ s}^{-1}$  on a dark background. Bottom: same as top for a Tm3 neuron. **b**, Top: response of a Tm1 neuron to a black bar moving rightwards, upwards, leftwards and downwards at  $100^{\circ} \text{ s}^{-1}$  on a

light background. Bottom: same as top for a Tm2 neuron. **c**, Average amplitude of the voltage response as a function of angle ( $0^{\circ}, 90^{\circ}, 180^{\circ}$  and  $270^{\circ}$ ) for Mi1 ( $n = 2$ ), Tm3 ( $n = 2$ ), Tm1 ( $n = 2$ ) and Tm2 ( $n = 3$ ) for a bar moving at  $100^{\circ} \text{ s}^{-1}$  (solid lines) and  $400^{\circ} \text{ s}^{-1}$  (dashed lines). The response amplitude was independent of the direction of motion in all cases.



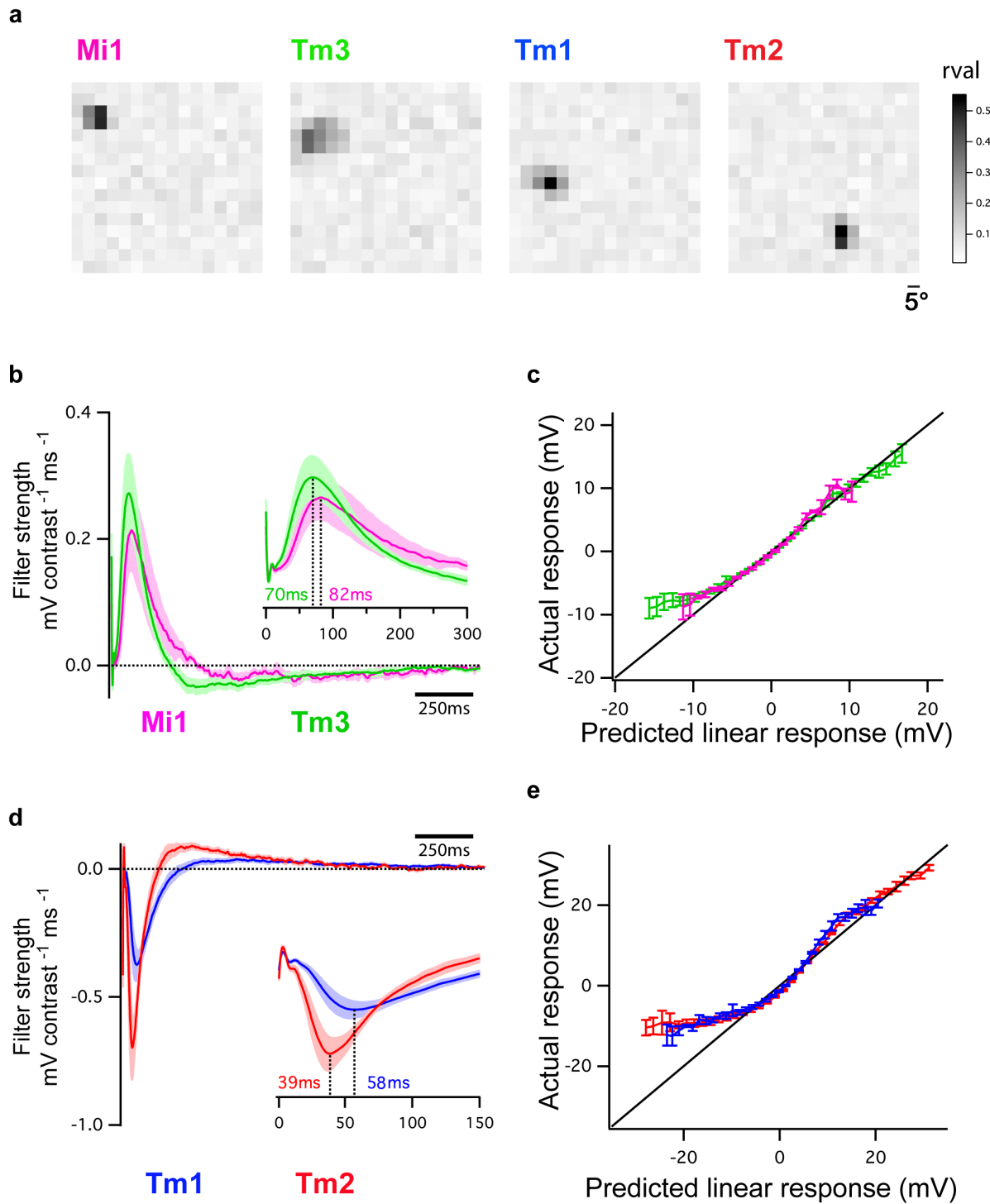
**Extended Data Figure 4 | The response of Mi1, Tm3, Tm1 and Tm2 to a Gaussian noise stimulus is very reliable.** **a**, Left: response of an Mi1 neuron to three consecutive 10 s presentations of an approximate Gaussian noise stimulus with 50% standard deviation and correlation time of 10 ms. Right: same as left for Tm3. **b**, Same as **a** for Tm1 (left) and Tm2 (right). **c**, Coherence of the measured responses in the four cell types. Deviations from 1 mean that variance

in the output is not entirely accounted for by a linear transformation of the input. This can be caused by noise in the response unrelated to the input, or by the nonlinearities in the system response that we measured. The linear filter amplitude for each frequency is distinct from coherence, and those amplitudes as a function of frequency are plotted in Extended Data Fig. 7a, b.



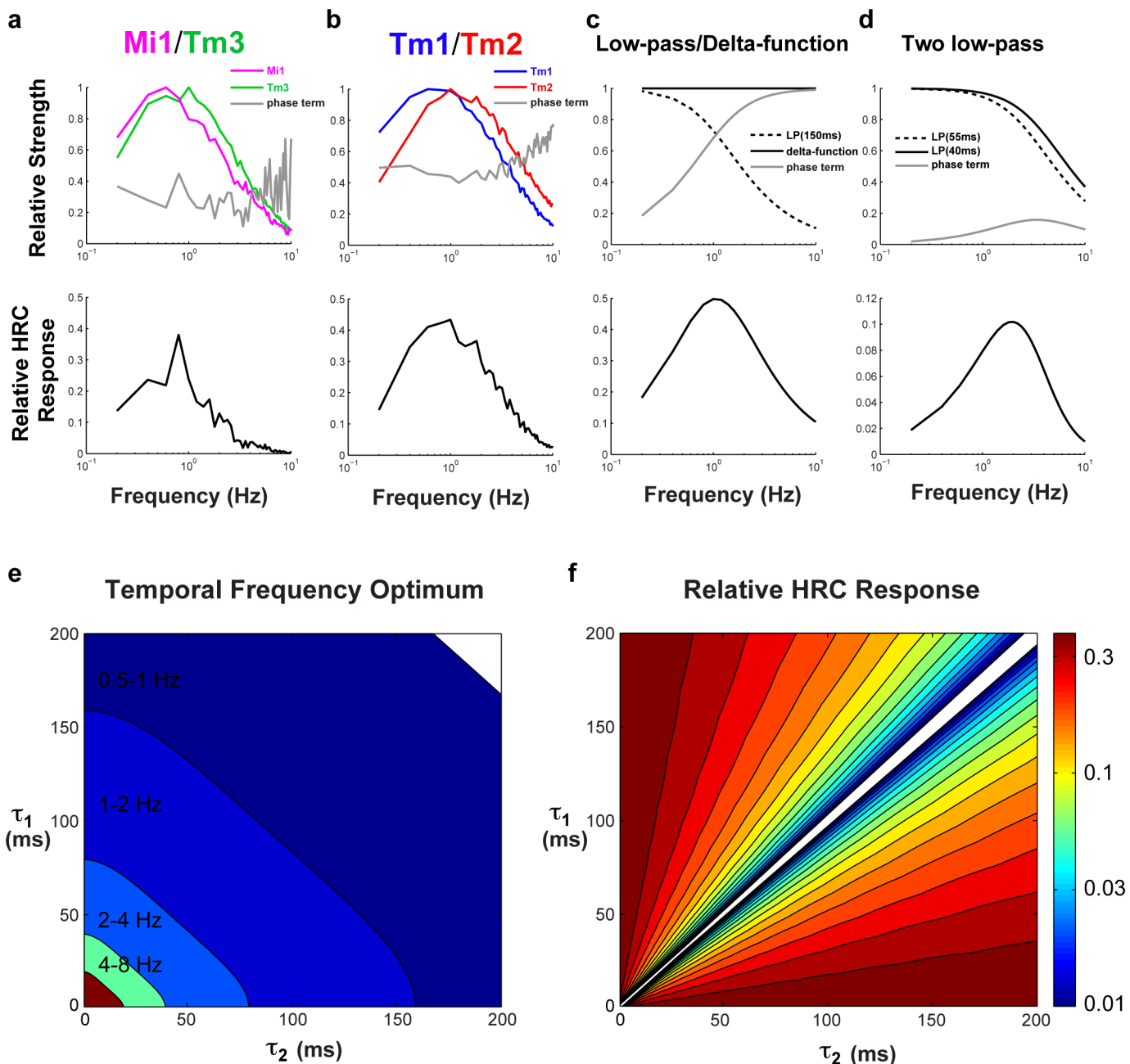
**Extended Data Figure 5 | Individual filters and nonlinearities from the Gaussian noise analysis of Mi1, Tm3, Tm1 and Tm2.** **a**, Individual filters (in grey) overlaid on the average filter ( $\pm$  s.e.m.) for Mi1 neurons. **b**, Individual

nonlinearities (in grey) overlaid on the averaged nonlinearity ( $\pm$  s.e.m.) for Mi1 neurons. **c, d**, Same as **a** and **b** for Tm3. **e, f**, Same as **a** and **b** for Tm1. **g, h**, Same as **a** and **b** for Tm2.



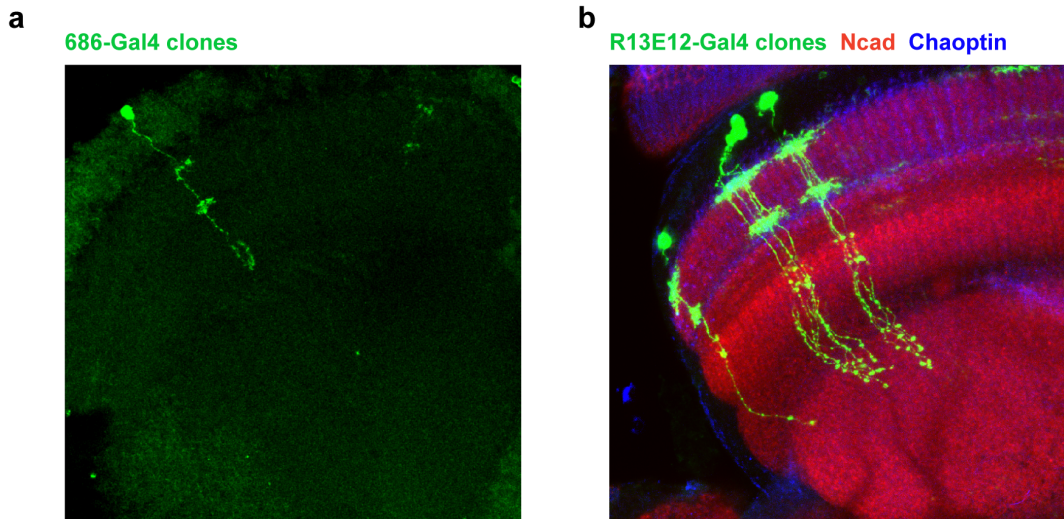
**Extended Data Figure 6 | Spatio-temporal analysis of Mi, Tm3, Tm1 and Tm2.** **a**, Representative receptive fields of Mi1, Tm3, Tm1 and Tm2 neurons shown as a heat map of 256 pixels using the  $r$  value of linear prediction for each pixel intensity. **b**, Average temporal filters ( $\pm$  s.e.m.) extracted from the highest responding pixels for each neuron for Mi1 ( $n = 4$ ) and Tm3 ( $n = 8$ ) (see Methods). The peaks of the filters, with the average timing, are enlarged in the

inset. **c**, Average nonlinearities over several neurons for both Mi1 and Tm3. To obtain each neuron's nonlinearity, the neuron's measured response was plotted against the linear prediction from the relevant pixels. Error bars, s.e.m. A line of slope 1 is shown in black. **d, e**, Equivalent to **b** and **c** for Tm1 ( $n = 8$ ) and Tm2 ( $n = 7$ ).



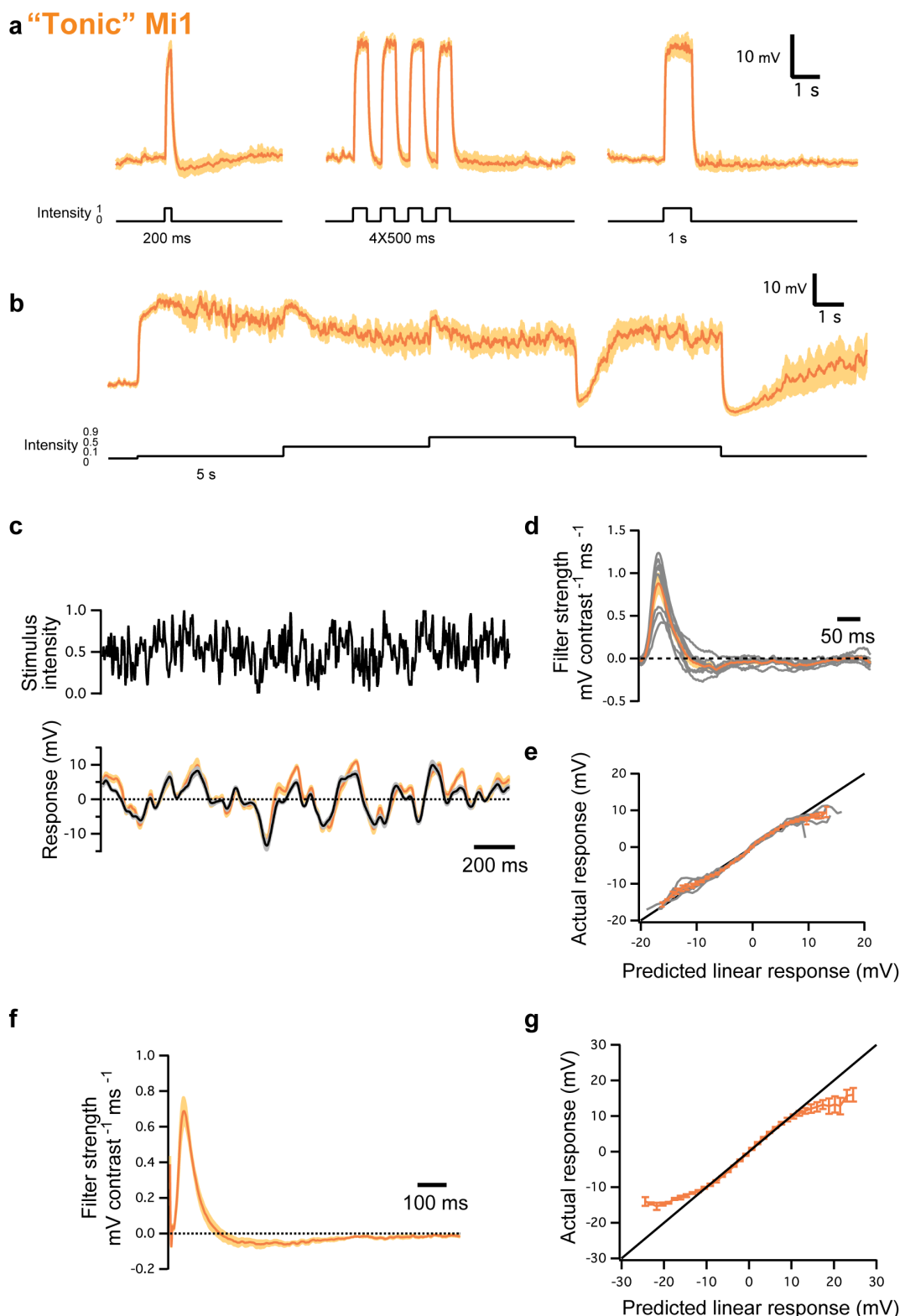
**Extended Data Figure 7 | Numerical and analytical HRC responses.** **a, b**, We plot three terms in equation (2) of the Methods, and the total HRC response, using the empirical measurements for Tm1/Tm2 and Mi1/Tm3 as the two input arms for the correlator ( $f_2(t)$ ) and  $f_1(t)$ , respectively). The analytical results computed here match the numerical ones shown in Fig. 4. Here and in all subsequent plots, we normalize the filter values so that they have a maximum of 1, and compute the relative HRC response from those normalized filters and the phase term. **c**, The same three components of equation (2) are plotted in the special case where  $f_1(t) = \delta(t)$  and  $f_2(t) = \frac{1}{\tau} e^{-t/\tau}$ . We plot the result with  $\tau = 150$  ms, so that the peak response occurs at  $\sim 1$  Hz. **d**, The same components of equation (2) are plotted in the case where both  $f_1(t)$  and  $f_2(t)$  are first-order low-pass filters, with time constants of 40 ms and 55 ms,

respectively. **e**, False-colour plot of the temporal frequency optimum for various combinations of  $\tau_1$  and  $\tau_2$ . Many combinations result in frequency optima near 1 Hz. **f**, The value of the relative HRC response at the optimal frequency in **e** is plotted for those same combinations of  $\tau_1$  and  $\tau_2$ . To compute this, temporal filters have a maximum gain of 1, as in **a-d**. The responses become small primarily when the phase term becomes small. When the phase term is very small, the subtraction performed by the HRC is susceptible to noise, since it can be subtracting two larger numbers to yield the small difference. Therefore, filter combinations with very small differences seem less biologically plausible than those with larger phase terms. The phase terms for the two model HRCs in **a** and **b** are between 0.2 and 0.4 in the 1-Hz region, larger than for the toy model shown in **d**.



**Extended Data Figure 8 | 686-Gal4 labels Mi1 neurons and R13E12-Gal4 is specific to Tm3 neurons.** **a**, Confocal image of a single Mi1 neuron obtained through a flip-out clone procedure with 686-Gal4. Mi1 neurons present processes at the level of M1 and M5 and terminate in the most proximal layers of the medulla. This line also sparsely labels Tm2 neurons, which were

distinguishable both visually and functionally. **b**, Confocal image of twin-spot MARCM clones obtained using R13E12-Gal4. Tm3 neurons present processes at the medulla layers M1 and M5 and project to proximal layers of the medulla and superficial layers of the lobula.



**Extended Data Figure 9 | Evoked response of 'tonic' Mi1 neurons.**

**a**, Average evoked responses ( $\pm$  s.e.m.) of 'tonic' Mi1 ( $n = 9$ ) in response to 200 ms, four consecutive 250 ms and 1 s full-field flashes of light from dark.

**b**, Average evoked responses ( $\pm$  s.e.m.) of 'tonic' Mi1 ( $n = 7$ ) in response to 5 s steps of light. **c**, Top: 2 s excerpt of the intensity signal from the 10 s full-field Gaussian noise stimulus. Correlation time is 10 ms. Bottom: average voltage response ( $\pm$  s.e.m.) of 'tonic' Mi1 ( $n = 8$ ) in response to the 2 s noise stimulus on top. The black trace corresponds to the average predicted linear response obtained by convolving the stimulus with the filters in **d** ( $\pm$  s.e.m.). **d**, Average temporal filters ( $\pm$  s.e.m.) extracted from the data in **c** that best predict the

measured response of 'tonic' Mi1 as a function of contrast history. Individual filters are shown in grey. **e**, Nonlinearities for 'tonic' Mi1 cells. Actual responses are plotted against their linear predicted responses. Individual cell nonlinearities in grey; mean and s.e.m. are represented by the coloured line and patch. A line of slope 1 is shown in black. **f**, Average temporal filters ( $\pm$  s.e.m.) extracted from the highest-responding pixels for each 'tonic' Mi1 neuron in the spatio-temporal experiments. **g**, Averaged actual responses of 'tonic' Mi1 plotted against their averaged linear predicted responses in the spatio-temporal experiments. Error bars, s.e.m. A line of slope 1 is shown in black.